RSC Advances

ROYAL SOCIETY OF CHEMISTRY

www.rsc.org/advances

Table of Contents Entry

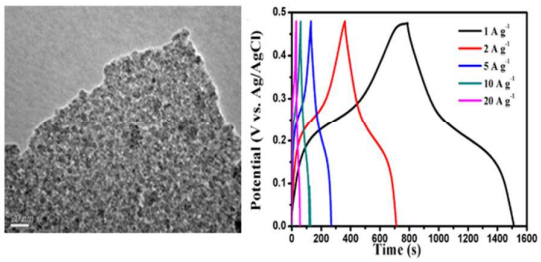

A facile one-pot refluxing method was developed to prepare nickel-cobalt sulfide ($NiCo_2S_4$) nanoparticles attached on reduced graphene oxide (RGO) nanosheets. The as-synthesized $NiCo_2S_4$/RGO hybrids as electrode materials for supercapacitors exhibit excellent electrochemical performance.

Journal Name

RSCPublishing

ARTICLE

Facile synthesis of nickel-cobalt sulfide/reduced graphene oxide hybrid with enhanced capacitive performance

Cite this: DOI: 10.1039/x0xx00000x

Xiaoqing Cai, Xiaoping Shen,* Lianbo Ma, Zhenyuan Ji, and Lirong kong

Received 00th January 2012,
Accepted 00th January 2012

DOI: 10.1039/x0xx00000x

www.rsc.org/

A uniform hybrid with nickel-cobalt sulfide ($NiCo_2S_4$) nanoparticles attached on reduced graphene oxide (RGO) nanosheets is fabricated through a facile one-pot refluxing method. $NiCo_2S_4$ nanoparticles with sizes of several nanometers uniformly disperse on the surface of RGO sheets, and the electrochemical property of the resulted $NiCo_2S_4$/RGO hybrids is investigated as electrode materials for supercapacitor. The $NiCo_2S_4$/RGO hybrids deliver a maximum specific capacitance of 1526 F g^{-1} at the current density of 1.0 A g^{-1}, and a great rate capability, remaining 1109 F g^{-1} at a high current density of 20 A g^{-1}. Moreover, after 2000 charge-discharge cycles at the current density of 10 A g^{-1}, 83% of the initial capacitance is maintained, indicating a good cycling stability The enhanced capacitive performance can be attributed to the synergistic effect between $NiCo_2S_4$ nanoparticles and RGO, in which RGO can serve as conductive channels and an ideal support matrix. The facile synthesis and the remarkable capacitive performance of the $NiCo_2S_4$/RGO hybrid make it a promising candidate for electrode material in electrochemical energy conversion/storage devices.

Introduction

In recent years, due to the rapid economic development and the depletion of fossil fuels, the demand for alternative energy conversion/storage devices with high power and energy densities is greatly increased. Among the multitudinous energy conversion/storage devices, supercapacitors attract a great attention owing to their high power density, good cycling stability, fast charge-discharge rates and low cost compared to lithium-ion batteries and traditional capacitors.[1,2] Electrode materials are the main contributor of electrical energy storage of supercapacitors. At present, carbonaceous materials, metal oxides and conductive polymers have been widely used as supercapacitor electrode materials.[3,4] The carbonaceous materials with high specific area and superior conductivity are usually used as working electrodes for Electrochemical Double Layer Capacitors, in which the electrical charge is a physical charge separation stored at the interfaces between the electrode and electrolyte.[2,5] Though they own many advantages such as excellent stability and low cost, their low capacitance (100-200 F g^{-1}) cannot meet the requirement for the high energy density of electrical devices.[6,7] In contrast, metal oxides and conductive polymers store energy by using interfacial reversible Faradaic reactions, which can provide much higher specific capacitance than those of Electrochemical Double Layer Capacitors.[8,9] Although the great specific capacitance has been reported recently, the severe degradation of conductive polymers greatly restricts their application as electrode materials for supercapacitors. Moreover, metal oxides have poor electrical conductivity and always suffer from relatively lower energy output. Therefore, the development of novel faradaic electrode materials with excellent capacitive performance is still a major challenge for the practical application of supercapacitors.

Recently, transition-metal sulfides have been demonstrated as a new type of faradaic electrode materials with excellent capacitive performance. For instances, Lou *et al.* obtained tube-like CoS_2 cavities by using a moderate solvothermal method and the product delivered a high capacitance of 980 F g^{-1} at 1.0 A g^{-1}.[10] Zheng *et al.* reported the flower-like β-NiS with a high capacitance of 858 F g^{-1} at 2.0 A g^{-1}.[11] Especially, nickel-cobalt sulfide ($NiCo_2S_4$), a binary transition-metal sulfide, has recently been considered as a promising electrode material for supercapacitors.[12,13] $NiCo_2S_4$ can offer richer redox reactions than the corresponding single-metal sulfides owing to the contributions of both nickel and cobalt with different valence states.[2,14] In addition, in comparison with its oxide counterpart of $NiCo_2O_4$, $NiCo_2S_4$ possess many advantages such as relatively higher conductivity[13] and more flexible structure, which make it easy for the electrons to transport,[15,16] and prevent it from being disintegrated. It was reported that the

porous $NiCo_2S_4$ nanotubes exhibit a high specific capacitance of 933 F g^{-1} at 1.0 A g^{-1},[12] and the urchin-like nanostructured $NiCo_2S_4$ shows a capacitance up to 1050 F g^{-1} at 2.0 A g^{-1}.[13] However, the preparation of $NiCo_2S_4$ usually adopts a complicated two-step approach,[2,3,13,17,18] which would increase the cost of production. Moreover, the $NiCo_2S_4$ products often show a severe agglomeration, which decreases the capacitive performance. Therefore, further efforts are needed to develop $NiCo_2S_4$ electrode materials with low production cost and improved electrochemical performance.

It is well-known that the introduction of carbonaceous materials into electrochemical active components can effectively improve the electrochemical performances of the hybrids.[19,20] Compared with zero-dimensional (0-D) carbon nanoparticles and one-dimensional (1-D) carbon nanotubes, 2-D graphene with outstanding electronic conductivity, large specific surface area and high thermal/chemical stability has been demonstrated to be a more favorable matrix for the dispersion of active components and the construction of conductivity networks so as to improve the electrochemical performance.[21-23] In this paper, we report a facile one-pot refluxing method to fabricate $NiCo_2S_4$/RGO (RGO = reduced graphene oxide) hybrid as electrode materials for supercapacitor, and demonstrate its excellent electrochemical performance with high specific capacitance, good rate capability and long cycle lifetime.

Experimental

Materials

Natural flake graphite with a particle size of 150 μm (99.9% purity) was purchased from Qingdao Guyu Graphite Co., Ltd. All of the other chemicals used in our experiments are commercially available analytical grade reagents, and used without further purification. Graphite oxide was synthesized from natural flake graphite using a modified Hummers method.[24,25]

Preparation of $NiCo_2S_4$/RGO hybrids

Typically, 20 mg of the prepared graphite oxide was dispersed in 60 ml of ethylene glycol (EG) through ultrasonication to form a homogeneous graphene oxide (GO) suspension. $Ni(Ac)_2{\cdot}4H_2O$ and $Co(Ac)_2{\cdot}4H_2O$ with a molar ratio of $n(Ni(Ac)_2{\cdot}4H_2O)/n(Co(Ac)_2{\cdot}4H_2O) = 1:2$ were added into the above suspension gradually, and then the solution was stirred at 80 °C for 2 h. Subsequently, 6 mmol of thiourea was introduced into the above solution. The resultant mixture was kept stirring for 1 h, and then was refluxed at 180 °C for 3 h. After the solution was cooled down to room temperature naturally, the product was collected by centrifugation, washed with deionized water and absolute ethanol for several times, and then dried in a vacuum oven at 45 °C for 12 h. The final products were designated as $NiCo_2S_4$/RGO-1, $NiCo_2S_4$/RGO-2, $NiCo_2S_4$/RGO-3 and $NiCo_2S_4$/RGO-4 for the feeding amount of 0.6 mmol, 0.8 mmol, 1.0 mmol and 1.2 mmol of $Ni(Ac)_2{\cdot}4H_2O$, respectively. For comparison, pure $NiCo_2S_4$ was synthesized in the absence of graphite oxide, and bare RGO was also prepared without $Ni(Ac)_2{\cdot}4H_2O$ and $Co(Ac)_2{\cdot}4H_2O$ but with other experimental parameters kept constant.

Instruments and characterization

Powder X-ray diffraction (XRD) was performed on a Bruker D8 Advance diffractometer with Cu K_α radiation (1.5406 Å) at a scanning rate of 7 °min^{-1}. The composition of the products was determined by energy-dispersive X-ray spectrometry (EDS). The morphology and size of the products were examined by a Hitachi S-4800 field emission scanning electron microscope (FESEM) and transmission electron microscopy (TEM, JEOL JEM-2100). Brunauer–Emmett–Teller (BET) surface areas of the products were tested using a surface area and porosity analyzer (NDVA-2000e). Raman scattering was collected at room temperature using a DXR Raman spectrometer with a 532 nm laser source.

Electrochemical measurements

Electrochemical measurements were performed on a three-electrode setup using a CHI 760D electrochemical analyzer (Chen Hua Instruments, Shanghai, China) at room temperature. Platinum foil and Ag/AgCl electrode were used as the counter and reference electrodes, respectively. The working electrodes were fabricated by mixing 80 wt% active materials ($NiCo_2S_4$/RGO, $NiCo_2S_4$ or RGO), 10 wt% acetylene black and 10 wt% poly(vinylidene fluoride) (PVDF) binder in *N*-methyl-2-pyrrolidone solvent, and then the mixture was stirred for about 24 h to form a homogeneous slurry. Subsequently, the slurry was pasted on the nickel foam substrates (surface area 1 cm^2) and then the nickel foam was placed into a vacuum oven and dried at 80 °C for 48 h. The electrodes loaded with the active material were then pressed at 10 MPa. The masses of the electrodes are about 1.6, 2.0, 1.8, 1.9, 1.7 and 1.2 mg for $NiCo_2S_4$/RGO-1, $NiCo_2S_4$/RGO-2, $NiCo_2S_4$/RGO-3, $NiCo_2S_4$/RGO-4, $NiCo_2S_4$ and RGO electrodes, respectively. The electrochemical properties of the as-prepared materials were evaluated by cyclic voltammetry (CV), galvanostatic charge-discharge (CD) and electrochemical impedance spectroscopy (EIS) techniques with a 3.0 M KOH aqueous solution as the electrolyte solution. The average specific capacitance was mainly calculated from the galvanostatic CD curves according to the following equation:[2,26]

$$C_s = I\Delta t/(m\Delta V) \quad (1)$$

where C_s is the specific capacitance (F g^{-1}) of the electrodes, I is the charge and discharge current (mA), Δt is the discharging time (s), m is the mass of the electroactive material of the electrode (mg), and ΔV is the discharging potential drop (V).

Results and discussion

The formation of $NiCo_2S_4$/RGO hybrids

In this work, we prepared $NiCo_2S_4$/RGO hybrids through a facile refluxing method (Scheme 1). During the synthesis process, homogeneous GO suspension was firstly prepared by

ultrasonication. Due to the ionization of the carboxylic-acid and phenolic hydroxyl groups on the edges and surfaces, GO nanosheets were highly negatively charged when dispersed in EG.[27] When $Ni(Ac)_2 \cdot 4H_2O$ and $Co(Ac)_2 \cdot 4H_2O$ were added into

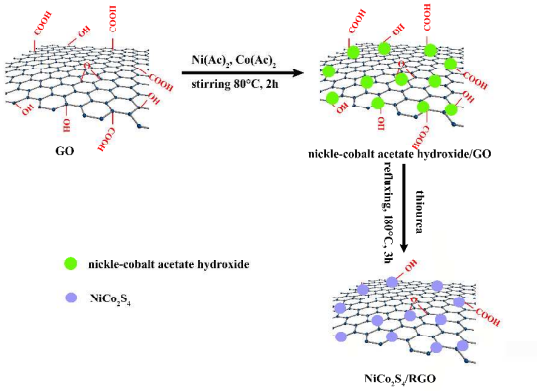

Scheme 1. Schematic illustration of the formation process of $NiCo_2S_4$/RGO hybrids.

the GO solution, Ni^{2+} and Co^{2+} ions were absorbed onto the surface of GO nanosheets through electrostatic interaction between positively charged metal ions and the negatively charged oxygen-containing groups. When the solution was kept stirring at 80 °C for 2 h, nickle-cobalt acetate hydroxide as an intermediate product was in-situ formed on GO sheets due to the hydrolysis of Ni^{2+} and Co^{2+} ions.[17] Then, thiourea was added into the reaction mixture and refluxed at 180 °C for 3 h to transform the intermediate into $NiCo_2S_4$. During the reaction process, EG acts as both the reaction solvent and the reductant to make GO converted into RGO.[28] Finally, $NiCo_2S_4$/RGO hybrid with $NiCo_2S_4$ nanocrystals uniformly anchored on RGO sheets was successfully obtained.

Structural and morphological characterization

The phase structures of the as-obtained products were characterized by XRD, and the results are shown in Fig. 1a.

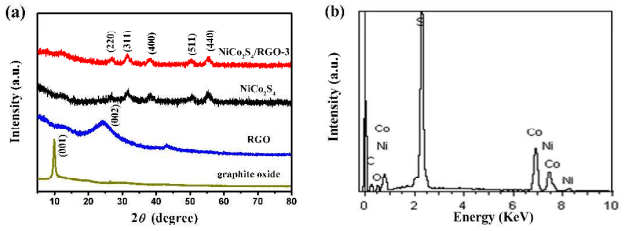

Fig. 1 (a) XRD patterns of graphite oxide, RGO, $NiCo_2S_4$ and $NiCo_2S_4$/RGO-3 hybrid; (b) The EDS spectrum of $NiCo_2S_4$/RGO-3 hybrid.

It can be seen clearly that the XRD pattern of graphite oxide shows a sharp diffraction peak at 2θ = 10.3º, corresponding to the characteristic (001) peak of graphite oxide.[29] The disappearance of (001) peak of graphite oxide and the emergence of (002) peak at 2θ = 24.1º in the XRD pattern of RGO demonstrate that graphite oxide has been well reduced to RGO during the synthesis process.[27,30] The wide and weak (002) reflection is typical for randomly ordered (turbostratic) graphitic structure[30]. It is seen that $NiCo_2S_4$/RGO-3 hybrid shows a similar XRD pattern as that of the pure $NiCo_2S_4$, and the peaks at 2θ values of 26.9º, 31.8º, 38.6º, 50.2º and 55.7º can be indexed to the (220), (311), (400), (511) and (440) reflections of cubic phase $NiCo_2S_4$ (JCPDS 20-0782), and no other diffraction peaks were detected, indicating that the presence of GO does not influence the crystal structure of the synthesized $NiCo_2S_4$ and the synthesized $NiCo_2S_4$ is of pure phase. The broad diffraction peaks indicate that the $NiCo_2S_4$ has tiny particle size. The disappearance of the (002) peak of RGO at 2θ = 24.1º may be attributed to the low content of RGO in $NiCo_2S_4$/RGO-3 hybrid and/or the forestalled stack of RGO sheets due to the attachment of $NiCo_2S_4$ nanoparticles on them.[31]

The EDS spectrum of $NiCo_2S_4$/RGO-3 hybrid is presented in Fig. 1b. The detectable elements in the hybrid include C, O, Ni, Co and S. The carbon element originates from RGO and the oxygen element comes from the residual oxygen-containing groups on RGO. Compared with Ni, Co and S, lower atomic percentages of C and O elements indicate the low content of RGO. In addition, the atomic ratio of Ni to Co was detected to be about 1:2, which is consistent with the initial molar ratio of Ni to Co used in the synthesis."

The morphology, size and microstructure of as-synthesized products were investigated by FESEM, TEM and high resolution TEM (HRTEM). FESEM images of $NiCo_2S_4$/RGO-3 hybrid reveal the presence of $NiCo_2S_4$ nanoparticles and silk-like RGO sheets (Fig. S2 see Supporting Information). The corresponding (HR) TEM images of the $NiCo_2S_4$/RGO-3 sample are shown in Fig. 2. The typically rippled and

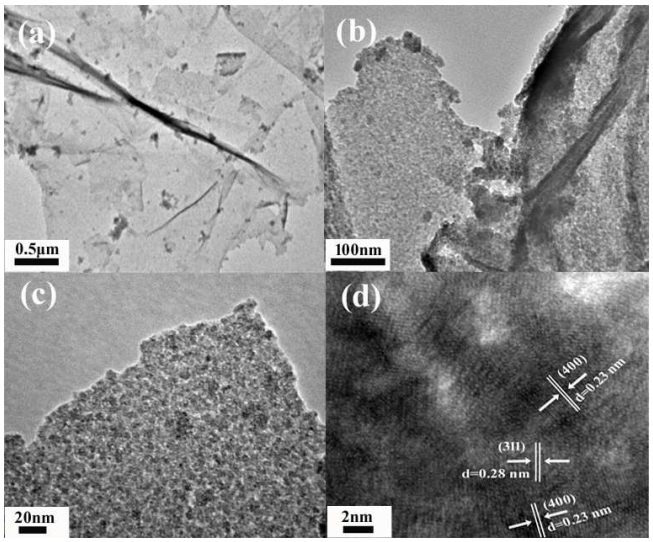

Fig. 2 (a-c) TEM images and (d) HRTEM image of $NiCo_2S_4$/RGO-3 hybrid.

crumpled structure of graphene sheets can be clearly seen from Fig. 2a, indicating the presence of RGO sheets in the hybrid. A more revealing feature of $NiCo_2S_4$/RGO-3 hybrid can be

observed from TEM images with higher magnifications (Fig. 2b and Fig. 2c), in which RGO sheets are covered by a uniform layer of nanoparticles with sizes of several nanometers. The high uniformity of the hybrid structure suggests a good combination between the nanoparticles and RGO. The HRTEM image (Fig. 2d) shows clear lattice fringes, and the lattice spacings of 0.28 and 0.23 nm correspond to the (311) and (400) planes of cubic $NiCo_2S_4$, respectively, further confirming the successful preparation of $NiCo_2S_4$/RGO hybrid. The TEM images of pure $NiCo_2S_4$ sample are present in Fig. S2 (see Supporting Information), from which it can be observed that $NiCo_2S_4$ nanoparticles agglomerate seriously. Moreover, nitrogen adsorption and desorption isotherms reveal that the specific surface areas of pure $NiCo_2S_4$ and $NiCo_2S_4$/RGO-3 hybrid are 25.0 and 34.1 m^2/g, respectively (Fig. S3 see Supporting Information). This result indicates that the integration with RGO can improve the specific surface area of $NiCo_2S_4$/RGO-3 hybrid. Therefore, more active surface of the active component is accessible by the electrolyte, which could contribute to an improvement of the electrochemical performance.

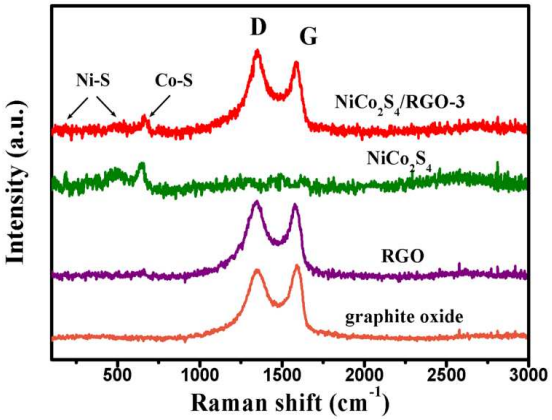

Fig. 3 Raman spectra of graphite oxide, RGO, $NiCo_2S_4$ and $NiCo_2S_4$/RGO-3 hybrid.

Raman spectroscopy is a powerful optical method to evaluate the structures of graphene-based materials, such as the disordered and defective structures. Fig. 3 displays the typical Raman spectra of graphite oxide, RGO, $NiCo_2S_4$ and $NiCo_2S_4$/RGO-3 hybrid. Except $NiCo_2S_4$, all spectra show two prominent peaks, corresponding to the well-defined D and G bands, respectively.[32] The D band at about 1345 cm^{-1}, derives from a breathing k-point phonon with A_{1g} symmetry, and is associated with structural defects and disorders, while the G band, centered at 1587 cm^{-1}, usually originates from the E_{2g} phonon of C sp^2 atoms, corresponding to stretching vibrations in the basal plane of graphene.[33] In general, the integrated peak intensity ratio of D to G band (I_D/I_G) is usually used to estimate the structural defects and disorders in the graphitic structures.[33] The I_D/I_G values of graphite oxide, RGO and $NiCo_2S_4$/RGO-3 hybrid are ca. 1.96, 2.18 and 2.19, respectively. The increase in I_D/I_G values for RGO and $NiCo_2S_4$/RGO-3 hybrid suggests that more disordered and defective carbon materials are obtained, further confirming that GO has been well deoxygenated and reduced during the synthesis process.[14] In addition, three weak peaks at 188.2 cm^{-1}, 513.8 cm^{-1} and 652.7 cm^{-1} can be observed in $NiCo_2S_4$ and $NiCo_2S_4$/RGO-3, which correspond to Ni-S and Co-S vibrational modes, respectively,[8,34] further confirming the presence of $NiCo_2S_4$ in the hybrids.

Electrochemical properties of $NiCo_2S_4$/RGO hybrids

The capacitive performances of supercapacitor electrodes based on $NiCo_2S_4$/RGO hybrids and $NiCo_2S_4$ were firstly investigated by CV in 3 M KOH aqueous solution with a three-electrode system. The shapes of CV curves clearly reveal the faradaic behavior, which is distinct from electric double-layer capacitance characterized by nearly rectangular CV curves.[20] Particularly, a pair of redox peaks can be observed from each curve, which may mainly result from the Faradaic redox reactions within the electrode materials. The redox reactions in $NiCo_2S_4$/RGO hybrid electrodes can be described in following equations:[5,35]

$$NiCo_2S_4 + OH^- + H_2O \text{ —— } NiSOH + 2CoSOH + 2e^- \quad (2)$$

$$CoSOH + OH^- \text{ —— } CoSO + H_2O + e^- \quad (3)$$

Fig. 4a shows the representative CV shapes of $NiCo_2S_4$/RGO hybrids and $NiCo_2S_4$ electrodes at a scan rate of 5 mV s^{-1}.

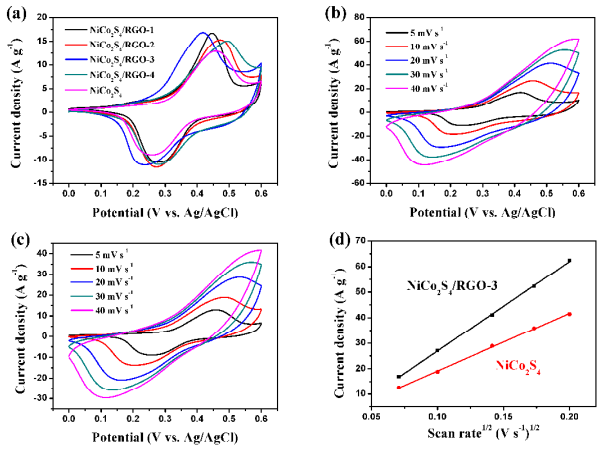

Fig. 4 (a) CV curves of $NiCo_2S_4$/RGO hybrids and $NiCo_2S_4$ electrodes at the scan rate of 5 mV s^{-1}; CV curves of (b) $NiCo_2S_4$/RGO-3 electrode and (c) $NiCo_2S_4$ electrode at various scan rates; (d) The variation of the current densities of the anodic peaks for $NiCo_2S_4$/RGO-3 and $NiCo_2S_4$ electrodes as a function of the square root of scan rate.

Based on the CV curves, the specific capacitance of the electrodes can be calculated by the formula: $C_s = (\int IdV)/(vm\Delta V)$, where I is the response current, ΔV is the potential difference, v is the potential scan rate, and m is the mass of the active materials in the electrodes.[20] It can be seen that specific capacitance is proportional to the area enclosed by CV curve. In comparison with the $NiCo_2S_4$ electrode, the $NiCo_2S_4$/RGO electrodes exhibit bigger mathematic areas of CV curves (Fig. 4a), indicating the $NiCo_2S_4$/RGO electrodes possess higher specific capacitances. Fig. 4b shows CV curves

of $NiCo_2S_4$/RGO-3 electrode at various scan rates. With the increase of scan rate, the potentials of the oxidation peak and reduction peak shift to the positive and the negative directions, respectively. The specific capacitance of $NiCo_2S_4$/RGO-3 hybrid is calculated to be 1023, 884, 692, 547 and 440 F g^{-1} at the scan rate of 5, 10, 20, 30 and 40 mV s^{-1}, respectively. Obviously, $NiCo_2S_4$/RGO-3 hybrid shows a gradual decrease of the specific capacitance with the increasing scan rate, which may be attributed to the diffusion effect limiting the diffusion and migration of the electrolyte ions within the electrode. When the scan rate increases, the rate of alkali ion transfer becomes relatively slow, and thus only the outer active surface of the electrode material can be utilized for charge storage during the redox process, resulting in a decrease in capacitance.[36] For comparison, the CV measurements of pure $NiCo_2S_4$ were also conducted and the CV curves at various scan rates are shown in Fig. 4c. The specific capacitances of $NiCo_2S_4$ at the scan rate of 5, 10, 20, 30 and 40 mV s^{-1} are *ca*. 685, 593, 451, 355 and 288 F g^{-1}, respectively. Thus, pure $NiCo_2S_4$ shows much smaller specific capacitance than $NiCo_2S_4$/RGO-3 under the same scan rate. From Fig. 4d, it can be seen that the anodic peak current is linearly proportional to the square root of scan rate. This reveals that the electrode reactions in both $NiCo_2S_4$/RGO-3 and $NiCo_2S_4$ correspond to reversible process, indicating that the specific capacitance is based on redox mechanism.[37] In addition, the slope is related to the diffusion coefficient of electrolyte ions.[38] The slope of $NiCo_2S_4$/RGO-3 electrode is larger than pure $NiCo_2S_4$ electrode, revealing more favorable ion diffusion in $NiCo_2S_4$/RGO-3 hybrid electrode.

To further evaluate the electrochemical properties of the as-prepared $NiCo_2S_4$/RGO hybrids, the galvanostatic CD measurements were carried out at the voltage window between 0 and 0.5 V, and the results are shown in Fig. 5. Fig. 5a presents the charge-discharge curves of the $NiCo_2S_4$/RGO hybrids and $NiCo_2S_4$ electrodes at a current density of 2.0 A g^{-1}. It should be noted that the discharge curves of $NiCo_2S_4$/RGO hybrids and $NiCo_2S_4$ show a plateaus at around 0.2 V, this indicates a typical faradaic behavior.[3,39] The specific capacitance can be calculated according to the equation (1). The calculated specific capacitance values for $NiCo_2S_4$/RGO-1, $NiCo_2S_4$/RGO-2, $NiCo_2S_4$/RGO-3, $NiCo_2S_4$/RGO-4, $NiCo_2S_4$ and RGO electrodes are 1010, 1080, 1484, 1273, 835 and 91 F g^{-1}, respectively. Obviously, $NiCo_2S_4$/RGO electrodes exhibit much higher specific capacitances than $NiCo_2S_4$ and RGO electrodes. This can be attributed to the synergistic effect between $NiCo_2S_4$ and RGO. With the RGO support, electron conduction paths can be created and thus the conductivities of $NiCo_2S_4$/RGO hybrids are greatly improved, which facilitates the charge transfer and charge transport during the redox reaction process.[40] Moreover, RGO can act as an effective matrix for the uniform dispersion of the $NiCo_2S_4$ nanoparticles, preventing the aggregation of $NiCo_2S_4$ nanoparticles, and thus effectively promotes the reaction between electrolyte and the active components.[28] Therefore, RGO in $NiCo_2S_4$/RGO hybrids serves as both conductive channel and an ideal support matrix. In addition, the optimal specific capacitance can be obtained through adjusting the loading amount of $NiCo_2S_4$ on RGO. It is observed that with the increase of $NiCo_2S_4$ content in $NiCo_2S_4$/RGO hybrids, the specific capacitance increases first and then decreases, and $NiCo_2S_4$/RGO-3 hybrid electrode owns the largest specific capacitance value among $NiCo_2S_4$/RGO hybrids. The increment of specific capacitance can be attributed to the increased content of active material ($NiCo_2S_4$) for capacitance generation. However, the increased content of $NiCo_2S_4$ will accordingly reduce the content of RGO, and thus the conductivity of $NiCo_2S_4$/RGO hybrids decreases, leading to the decrease of specific capacitance value. Therefore, a suitable content of $NiCo_2S_4$ in $NiCo_2S_4$/RGO hybrids is critical to obtain the optimal electrochemical performance.

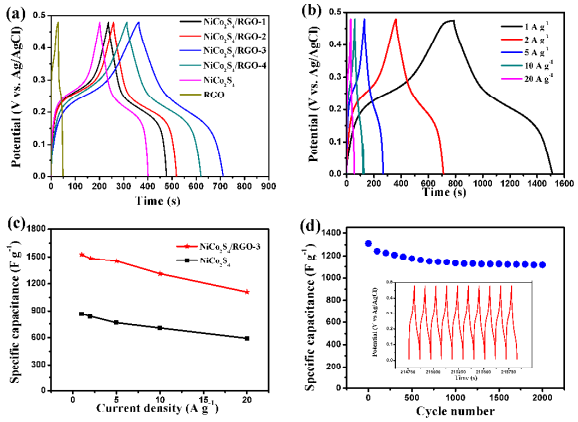

Fig. 5 (a) Charge-discharge curves of $NiCo_2S_4$/RGO hybrids, $NiCo_2S_4$ and RGO electrodes at the current density of 2.0 A g^{-1}; (b) charge-discharge curves of $NiCo_2S_4$/RGO-3 electrode at various current densities of 1.0, 2.0, 5.0, 10 and 20 A g^{-1}; (c) the specific capacitance values of $NiCo_2S_4$/RGO-3 hybrid and $NiCo_2S_4$ electrodes as a function of current density; (d) the cycling performance of $NiCo_2S_4$/RGO-3 hybrid electrode at a constant current density of 10 A g^{-1}. The inset of (d) shows the charge-discharge curves of the last 10 cycles.

Fig. 5b presents the charge-discharge curves of $NiCo_2S_4$/RGO-3 hybrid electrode at various current densities. It can be seen that the discharge time decreases with the increased current densities ranging from 1.0 to 20 A g^{-1}. The charge-discharge curves of other hybrids with different ratios of $NiCo_2S_4$ to RGO and pure $NiCo_2S_4$ at different current densities are displayed in Fig. S4 (see Supporting Information). The average specific capacitance values of $NiCo_2S_4$/RGO-3 hybrid and pure $NiCo_2S_4$ electrodes as a function of current density are plotted in Fig. 5c. Both plots descend with the increased current density. This phenomenon can be attributed to the fact that the diffusion of OH^- anion is not fast enough to reach the interface between the electrolyte and electrode during the charge-discharge process when a high current density is applied.[41] The $NiCo_2S_4$/RGO-3 hybrid electrode achieves the capacitance values of 1526, 1484, 1452, 1310 and 1109 F g^{-1} at current density of 1.0, 2.0, 5.0, 10 and 20 A g^{-1}, respectively. Impressively, almost 73% of the specific capacitance at 1.0 A g^1 is still retained when the current density is increased to 20 A g^{-1}. Compared with the previously reported result about $NiCo_2S_4$ nanosheets/graphene hybrid (rate capacitance retention

is about 52.4% from 3 to 20 A g^{-1}),[14] this work exhibits better rate capacitance.

The cycling stability of $NiCo_2S_4$/RGO-3 hybrid electrode was also investigated by repeating the charge-discharge measurement for 2000 cycles at a constant current density of 10 A g^{-1}. Fig. 5d presents the specific capacitance as a function of cycle number. It can be observed that the specific capacitance value decreases gradually to 1175.0 F g^{-1} at the 500th cycle, and then it remains stable in the residual cycles. The cycling stability is good with the specific capacitance retention of 83% after 2000 cycles. The inset of Fig. 5d shows the charge-discharge curves of the last 10 cycles, which indicates good long-term electrochemical cycling stability even under high current density.

Specific energy and specific power are two key factors for evaluating the electrochemical properties of supercapacitors. The energy density and power density values are calculated according to galvanostatic charge-discharge curves, and the equations are displayed as follows:

$$E = (C\Delta V^2)/2,\ P = E/t$$

where E (W h Kg^{-1}) is the average energy density, C (F g^{-1}) is specific capacitance, ΔV (V) is the potential window during discharge, P (W kg^{-1}) is the average power density, and t (s) represents the discharge time. As shown in Fig. 6, the energy

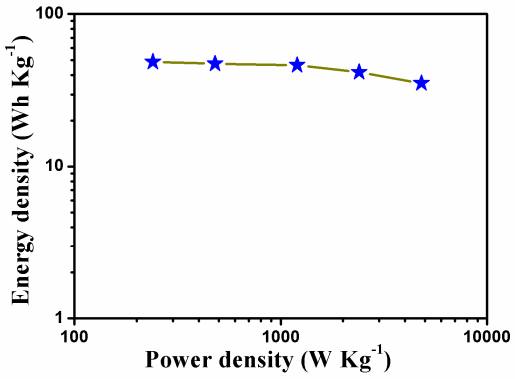

Fig. 6 Ragone plot of the estimated energy density and power density of $NiCo_2S_4$/RGO-3 hybrid electrode.

density of $NiCo_2S_4$/RGO-3 hybrid can reach to 48.8 W h Kg^{-1} at a power density of 239.9 W kg^{-1}, and still remains 35.5 W h Kg^{-1} at a much higher power density of 4801.6 W kg^{-1}, demonstrating promising application in supercapacitor electrode materials.

To further understand the electrochemical characteristic of electrode material, EIS was carried out at open circuit potential with an amplitude of 5 mV in the frequency range of 100 KHz to 0.1 Hz. The Nyquist plots of $NiCo_2S_4$/RGO-3 hybrid, $NiCo_2S_4$ and RGO are shown in Fig. 7a, and the equivalent circuit that employed to fit the EIS spectra is presented in the inset of Fig. 7a, where R_s represents the resistance related to the ionic conductivity of the electrolyte and electronic conductivity of the electrodes and current collectors; Q is the constant phase element accounting for a double-layer capacitance; R_{ct} is the charge-transfer resistance associated with the Faradic reactions; W is the Warburg resistance arise from the ion diffusion and transport in the electrolyte, and C_L is the limit capacitance.[16,42]

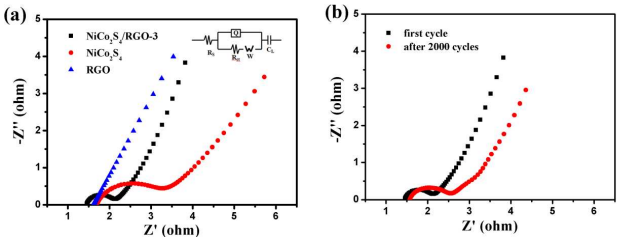

Fig. 7 (a) Nyquist plots of $NiCo_2S_4$/RGO-3 hybrid, $NiCo_2S_4$ and RGO electrodes; (b) Nyquist plots of the $NiCo_2S_4$/RGO-3 hybrid at the first and 2000th cycles.

A big semi-arc means a larger resistance of electrochemical reaction between electrode and electrolyte.[43] Based on the EIS data, it is found that the fitting R_{ct} (0.64 ohm) of $NiCo_2S_4$/RGO-3 hybrid electrode shows much smaller value than that of $NiCo_2S_4$ (1.54 ohm), which means easy electron transport in $NiCo_2S_4$/RGO-3 hybrid electrode. Compared with $NiCo_2S_4$, $NiCo_2S_4$/RGO-3 hybrid electrode has a more vertical line in the low frequency region, suggesting a more ideal capacitive behavior.[16,44] These results confirm that the electrochemical resistance of $NiCo_2S_4$ could be reduced by the incorporation of RGO. In addition, the Nyquist plots of the $NiCo_2S_4$/RGO-3 hybrid at the first and 2000th cycles were displayed in Fig. 7b. From the comparison of these two impedance curves, the $NiCo_2S_4$/RGO-3 hybrid after 2000 charge-discharge cycles has a bigger semi-arc and a lower slope than that at the first cycle, which can be ascribed to an enhancement of the charge-transfer resistance in the electrode reaction and a slower diffusion rate of ions between electrode and electrolyte after cycling.[2]

Conclusions

In conclusion, $NiCo_2S_4$/RGO hybrids with $NiCo_2S_4$ nanoparticles uniformly attached on RGO sheets have been fabricated through a facile one-pot refluxing method. The as-synthesized $NiCo_2S_4$/RGO hybrids as electrode materials for supercapacitors exhibit improved capacitive performance with a specific capacitance as high as 1526 F g^{-1} at the current density of 1.0 A g^{-1}, excellent rate capability with the specific capacitance of 1109 F g^{-1} at a high current density of 20 A g^{-1} and good cycling stability with 83% of the initial capacitance retention after 2000 cycles. These results are much better than those of the reported $NiCo_2S_4$ materials.[2,3,12-14] The enhanced capacitive performance can be attributed to the presence of RGO, which serves as both conductive channels to improve the poor electrical conductance, providing charge transfer pathways for $NiCo_2S_4$ nanoparticles, and an ideal matrix for the well-dispersion of $NiCo_2S_4$ nanoparticles. The facile synthesis and excellent electrochemical property of the $NiCo_2S_4$/RGO hybrids make them promising electrode materials for supercapacitor application.

Acknowledgements

The authors are grateful for financial support from Specialized Research Fund for the Doctoral Program of Higher Education of China (No. 20123227110018) and National Nature Science Foundation of China (No. 51272094).

Notes and References

School of Chemistry and Chemical Engineering, Jiangsu University, Zhenjiang 212013, People's Republic of China

1 J. Yan, Q. Wang, T. Wei and Z. J. Fan, *Adv. Energy Mater.,* 2014, **4**, 1300816.
2 J. Pu, F. L. Cui, S. B. Chu, T. T. Wang, E. H. Sheng and Z. H. Wang, *ACS Sustainable Chem. Eng.,* 2014, **2**, 809−815.
3 Y. F. Zhang, M. Z. Ma, J. Yang, C. C. Sun, H. Q. Su, W. Huang and X. C. D, *Nanoscale*, 2014, **6**, 9824-9830.
4 Y. J. Chen, B. H. Qu, L. L. Hu, Z. Xu, Q.H. Li and T. H. Wang, *Nanoscale*, 2013, **5**, 9812-9820.
5 J. W. Xiao, L. Wan, S. H. Yang, F. Xiao and S.Wang, *Nano. Lett.,* 2014, **14**, 831−838.
6 M. Kaempgen, C. K. Chan, J. Ma, Y. Cui and G. Gruner, *Nano. Lett.,* 2009, **9**, 1872−1876.
7 C. Huang, N. Grobert, A. A. R. Watt, C. Johnston, A. Crossley, N. P. Young and P. S. Grant, Carbon, 2013, **61**, 525−536.
8 J. Zhong, A. Wang, G. Li, J. Wang, Y. Ou and Y. Tong, *J. Mater. Chem.,* 2012, **22**, 5656–5665.
9 L. Wan, J. W. Xiao, F. Xiao and S. Wang, *ACS Appl. Mater. Interfaces,* 2014, **6**, 7735−7742.
10 L. Zhang, B. W. Hao and X. W. Lou (David), *Chem. Commun.,* 2012, **48**, 6912 –6914.
11 J. Q. Yang, X. C. Duan, Q. Qin and W. J. Zhen, *J. Mater. Chem. A,* 2013, **1**, 7880−7884.
12 H. Z. Wan, J. J. Jiang, J. W. Yu, K. Xu, L. Miao, L. Zhang, H. C. Chen and Y. J. Ruan, *CrystEngComm,* 2013, **15**, 7649-7651.
13 H. C. Chen, J. J. Jiang, L. Zhang, H. Z. Wan, T. Qi and D. D. Xia, *Nanoscale,* 2013, **5**, 8879-8883.
14 S. J. Peng, L. L. Li, C. C. Li, H. T. Tan, R. Cai, Yu H, S. Mhaisalkar, M. Srinivasan, S. Ramakrishna and Q. Y. Yan, *Chem. Commun.,* 2013, **49**, 10178–10180.
15 S. H. Park, Y. K. Sun, K. S. Park, K. S. Nahm, Y. S. Lee and M. Yoshio, *Electrochim. Acta,* 2002, **47**, 1721-1726.
16 Y. H. Li, L. J. Cao, L. Qiao, M. Zhou, Y. Yang, P. Xiao and Y. H. Zhang, *J. Mater. Chem. A,* 2014, **2**, 6540-6548.
17 L. Yu, L. Zhang, H. B. Wu and Lou XW (David), *Angew. Chem. Int. Ed.,* 2014, **53**, 3711-3714.
18 J. W. Xiao, X. W. Zeng, W. Chen, F. Xiao and S. Wang, *Chem. Commun.,* 2014, **50**, 9596.
19 M. J. Zhi, C. C. Xiang, J. T. Li, M. Li and N. Q. Wu, *Nanoscale,* 2013, **5**, 72-88.
20 W. M. Du, Z. Y. Wang, Z. Q. Zhu, S. Hu, X. Y. Zhu, Y. F. Shi, H. Pang and X. F. Qian, *J. Mater. Chem. A,* 2014, **2**, 9613-9619.
21 X. J. Liu, X. Qi, Z. Zhang, L. Ren, G. L. Hao, Y. D. Liu, Y. Wang, K. Huang, X. L. Wei, J. Li, Z. Y. Huang and J. X. Zhong, *RSC Adv.,* 2014, **4**, 13673-13679.
22 C. C. Xiang, M. Li, M. J. Zhi, A. Manivannan and N. Q. Wu, *J. Power Sources,* 2013, **226**, 65–70.
23 Q. H. Wang, L. F. Jiao, H. M. Du, Y. C. Si, Y.J. Wang and H. T. Yuan, *J. Mater. Chem.,* 2012, **22**, 21387–21391.
24 Z. Y. Ji, X. P. Shen, J. L. Yang, G. X. Zhu, K. M. Chen, *Appl. Catal. B,* 2014, **144**, 454-461.
25 W. S. Hummers and R. E. Offeman, *J. Am. Chem. Soc.,* 1958, **80**, 1339.
26 C. Z. Yuan, J. Y. Li, L. R. Hou, X. G. Zhang, L. F. Shen and X. W. D. Lou, *Adv. Funct. Mater.,* 2012, **22**, 4592-4597.
27 Z. Y. Ji, X. P. Shen, G. X. Zhu, H. Zhou and A. H. Yuan, *J. Mater. Chem.,* 2012, **22**, 3471–3477.
28 Q. Liu, J. T. Jin, J. Y. Zhang, *ACS Appl. Mater. Interfaces,* 2013, **5**, 5002−5008.
29 L. B. Ma, X. P. Shen, Z. Y. Ji, S. Wang, H. Zhou and G. X. Zhu, *Electrochim. Acta.,* 2014, **146**, 525-532.
30 A. B. Bourlinos, D. Gournis, D. Petridis, T. Szabo, A. Szeri and I. Dekany, *Langmuir,* 2003, **19**, 6050-6055.
31 Z. Y. Ji, G. X. Zhu, X. P. Shen, H. Zhou, C. M. Wu and M. Wang, *New J. Chem.,* 2012, **36**, 1774-1780.
32 Z. Zhang, X. J. Liu, X. Qi, Z. Y. Huang, L. Ren and J. X. Zhong, *RSC Adv.,* 2014, **4**, 37278-37283.
33 M. S. Dresselhaus, A. Jorio, M. Hofmann, G. Dresselhaus and R. Saito, *Nano Lett.,* 2010, **10**, 751-758.
34 Z. Zhang, Z. Y. Huang, L. Ren, Y. Z. Shen, X. Qi and J. X. Zhong, *Electrochim. Acta,* 2014, **149**, 316-323.
35 W. J. Dong, X. B. Wang, B. J. Li, L. N. Wang, B. Y. Chen, C. R. Li, X. A. Li, T. R. Zhang and Z. Shi, *Dalton Trans.,* 2011, **40**, 243-248.
36 W. M. Du, Z. Q. Zhu, Y. B. Wang, J. N. Liu, W. J. Yang, X. F. Qian and H. Pang, *RSC Adv.,* 2014, **4**, 6998-7002.
37 K. X. H, X. G. Z and J. L, *Electrochim. Acta,* 2006, **51**, 1289-1292.
38 C. S. Dai, P. Y. Chien, J. Y. Lin, S. W. Chou, W. K. Wu, P. H. Li, K. Y. Wu and T. W. Lin, *ACS Appl. Mater. Interfaces,* 2013, **5**, 12168-12174.
39 H. L. Wang, Q. M. Gao and L. Jiang, *Small,* 2011, **7**, 2454-2459.
40 H. Jiang, J. Ma and C. Z. Li, *Chem. Commun.,* 2012, **48**, 4465–4467.
41 M. Shahid, J. L. Liu, I. Shakir, M. F. Warsi, M. Nadeem and Yuk. Kwon, *Electrochim. Acta,* 2012, **85**, 243-247.
42 X. Wang, W. S. Liu, X. H. Lu and P. S. Lee, *J. Mater. Chem.,* 2012, **22**, 23114-23119.
43 J. W. Xiao and S. H. Yang, *J. Mater. Chem.,* 2012, **22**, 12253-12262.
44 M. D. Stoller, S. J. Park, Y. W. Zhu, J. H. An and R.S. Ruoff, *Nano Lett.,* 2008, **8**, 3498-3502.